Quaternary Geochronology 67 (2022) 101233

Contents lists available at ScienceDirect

Quaternary Geochronology

journal homepage: www.elsevier.com/locate/quageo

Quaternary ice thinning of David Glacier in the Terra Nova Bay region, Antarctica

Hyun Hee Rhee [a,d], Min Kyung Lee [b], Yeong Bae Seong [a,*], Jae Il Lee [b], Kyu-Cheul Yoo [b], Jamey Stutz [c], Byung Yong Yu [d]

[a] Department of Geography, Korea University, Seoul 02841, South Korea
[b] Division of Glacial Environmental Research, Korea Polar Research Institute, Incheon, 21990, South Korea
[c] Antarctic Research Centre, Victoria University of Wellington, PO Box 600, Wellington, 6140, New Zealand
[d] AMS Laboratory, Korea Institute of Science and Technology, Seoul, 02792, South Korea

ARTICLE INFO

Keywords:
Victoria land
Antarctica
Cosmogenic nuclides
Deglaciation
Mid-bruhnes event
Quaternary
Ross sea

ABSTRACT

Understanding the history of Antarctic glaciation is important for interpreting paleoclimatic changes and estimating the changes in climate, sea level, and ice volume in the future. Ice core studies of the East Antarctic Ice Sheet (EAIS) and marine sediment cores from the entire Ross Sea have employed numerous proxies to reconstruct the glacial history of the Antarctic region. However, the ice and marine core records can be biased because of their specific locations, such as the uppermost accumulation zone or the terminus of the ablation zone, thereby introducing significant uncertainties in ice modeling. In this study, we analyzed 34 new ^{10}Be and ^{26}Al samples from four benches that were glaciated in the past by David glacier and incorporate the present ice-free flat surfaces. We suggest that the David glacier experienced monotonic and stepwise vertical lowering along the flanks of Mt. Priestley since the early Pleistocene. The uppermost bedrock benches on Mt. Priestley were exposed at 1.77 ± 0.32 Ma, with no evidence of subsequent overriding by readvancing ice. At Mt. Priestley, the David glacier has been characterized by a cold-based regime since 1.77 Ma, with a denudation rate of only ~16 cm/Ma, corresponding to the regional transition from warm to cold-based glaciation at 3.5 Ma. Simple exposure ages from two lower benches date to Marine Isotope Stage (MIS) 7 (234.1 ± 13.1 ka; 545 m asl) and MIS 4 (64.8 ± 13.7 ka; 222 m asl), suggesting that, since MIS 8, the overall lowering of glaciers has remained monotonic. The upper bench marks the lower limit of the MIS 8 glacial period and the upper limit of Penultimate Glacial Maximum (MIS 6), while the lower landform defines the upper limit of the last glacial period (MIS 4–2). The magnitude of Quaternary ice thinning at the David glacier was the highest (~990 m) in the present terminal area (i.e., the most sensitive ablation zone), in contrast to the other outlet glaciers draining into the Terra Nova Bay, which experienced less ice lowering. The combination of the terrestrial (in situ ^{10}Be and ^{26}Al) and previous marine (authigenic ^{10}Be) cosmogenic data used in our study document the history of lowering of the David glacier driven by climatic changes during the Pleistocene. Both deglaciation and glaciation were limited during the mid-Pleistocene transition (MPT) and prior to the mid-Bruhnes event (MBE), due to the prevailing cold and arid climate, whereas deglaciation was dominant during other warm periods.

1. Introduction

Since the Oligocene, Antarctic ice sheets have played a central role in the global sea level and climate changes. Establishing the chronologies of these changes, with respect to the extent of ice sheet coverages, has remained a great challenge. The East Antarctic Ice Sheet (EAIS) is believed to have first appeared during the late Cenozoic Antarctic glaciation (~34 Ma), when ice expansion started occupying the existing network of fluvial valleys (Strand et al., 2003; Sugden and Denton, 2004; Baroni et al., 2005). The early periods of warm-based EAIS had dramatically modified the subglacial landscape, carving several U-shaped valleys, cirques, sharp ridges, spires, horns, and hanging ice valleys visible along the margins of the ice sheet today (Orombelli et al., 1990; Baroni et al., 2004, 2005). The transition to cold-based glaciation at ~14 Ma, which coincided with the global cooling episode during middle Miocene, promoted the further growth of EAIS and triggered the

* Corresponding author.
E-mail address: ybseong@korea.ac.kr (Y.B. Seong).

https://doi.org/10.1016/j.quageo.2021.101233
Received 25 March 2021; Received in revised form 16 September 2021; Accepted 17 September 2021
Available online 21 September 2021

extinction of the tundra community (Lewis et al., 2007, 2008). Since then, extremely low erosion (associated with hyper-arid conditions) have preserved paleo-meltwater scoured features on subglacial channel beds (Sugden et al., 1991; Denton and Sugden, 2005). The preserved cold-based glacial landforms on Roberts Massif of Transantarctic mountains since ~14.5 Ma and the persistent terrestrial ice sheets since 14 Ma also support the transition period (Levy et al., 2019; Balter et al., 2020).

Cosmogenic nuclide surface-exposure dating techniques have constrained the transition from warm to cold-based glaciation in Victoria Land and have established the continuous exposure of the highest surfaces and extremely low denudation rates in the entire region. The nunataks in Southern Victoria Land have been continuously exposed since 3.5 Ma (uncorrected for erosion), whereas the local mountain summits in northern Victoria Land have remained ice-free since 6 Ma (Oberholzer et al., 2003, 2008; Di Nicola et al., 2009, 2012; Strasky et al., 2009). In this study, we used paired cosmogenic nuclides (^{10}Be, ^{21}Ne, and ^{26}Al) to determine the precise glacial history of these ancient relict landscapes. The bedrocks and glacial erratics supplied from upstream or glacial valley walls were exposed to cosmogenic rays multiple times, and hence, they contain inherited or depleted isotopes, which leads to disturbed isotope ratios or statistically outlier ages in some samples (Heyman et al., 2011). A combination of stable and/or radioactive nuclides having different half-lives are widely used to detect the inheritance and/or reworking problems. These dating results not only provided the minimum transition period but also confirmed the absence of significant EAIS expansion during the Pleistocene (Di Nicola et al., 2009; Lilly et al., 2010). A marine study also revealed that colder events at ~3.3 Ma transited the EAIS to polar ice sheet and led to the expansion of the EAIS and the sea ice on Ross Embayment (ANDRILL AND-1B; McKay et al., 2012). The transited polar ice sheet on Ross Embayment shows no increase in its thickness since the Pleistocene, while marine ice sheets have repeatedly expanded and retreated in response to temperature fluctuations (Swanger et al., 2011; Levy et al., 2016).

Several studies on Victoria Land focused on the relatively recent periods during MIS 4–2 and identified the appearance of early or late local Last Glacial Maximum (local LGM), and not the global LGM (26–19 ka; Clark et al., 2009). Glaciers have maintained their maximum elevation in the Ross Sea Embayment (Southern Victoria Land) until the Late Glacial or Holocene period, lagged by the sea level rise event on Meltwater Pulse 1A (Jones et al., 2015; Anderson et al., 2017; Jackson et al., 2018; Christ and Bierman, 2020). The post-LGM deglaciations are largely associated with the retreat of the EAIS outlet glaciers on the Northern Victoria Land, reconstructed from subglacial topography and sea level changes that affected the marine ice sheet instability during late local LGM (Goehring et al., 2019; Rhee et al., 2020). Additional studies have indicated that the local LGM preceded the global LGM, both in the interior EAIS and around its periphery (Lilly et al., 2010; Rhee et al., 2019).

However, the respective timeframes proposed by such glacial reconstruction studies did not fully cover the Quaternary and are rather restricted to periods that are either too old (>1 Ma) or too young (<100 ka). Given the extensive horizontal and vertical variability of ice dynamics along a glacier's longitudinal profile (Wuite et al., 2009), a more detailed record of past glaciation can be obtained by sampling in multiple locations at different elevations near a single glacier system. In this study, we reported the glacial history reconstructed in the Terra Nova Bay region over the last ~2 Ma, a period spanning the Pleistocene that experienced monotonic ice sheet lowering. We conjugated the cosmogenic exposure dating with paired in-situ nuclides (^{26}Al & ^{10}Be) from four exposed benches on Mt. Priestley with ice lowering, located on the present terminal area of the David glacier. Climatic changes recorded in the most upstream (Dome C) and downstream (Southern Ocean) areas of the David Glacier were eventually compared to determine a more detailed glacial history.

2. Study area

Victoria Land, adjoining the western Ross sea, is presently surrounded by three major ice domes [Charlie (C), Taylor, and Talos], with the interior ice draining into Terra Nova Bay via numerous outlet glaciers. Among the outlet glaciers, David Glacier is the largest, where the interior EAIS converges at the David Cauldron and subsequently flows into the Drygalski ice tongue of the Terra Nova Bay (Fig. 1). The ice-free areas along the Victoria Land coast consist of glacially eroded surfaces, post-glacial erratic covers, and volcanic materials.

Mt. Priestley is located at the northern edge of David Cauldron and exhibits a series of benches exposed along the lateral margin of David Glacier (Figs. 1 and 2A and). The bedrock lithology of this area is granitic, and the glacial erratics covering the low-stand areas consist of various rock types, such as granite, quartzite, and volcanics. The summit of Mt. Priestly [~1100 m above sea level (asl)], which is devoid of erratic boulders, is composed of bedrock and regolith on flat surfaces surrounded by tors or peaks varnished with dark rocks (Fig. 2B). These surfaces have been heavily eroded by glacial plucking, polishing, and subsequent post-glacial denudation via periglacial processes (Fig. 2C and D ; Baroni, 1987; Bockheim and Hall, 2002). Flat high-elevation surfaces have developed between the rounded summits via cryoplanation, with their bedrock fragments exhibiting highly weathered pits or tafoni (Fig. 2F). Steep slopes are confined to cirque walls, cliffs, and tors located along the surface margins; notably, in this area, paraglacial processes cause occasional rockfalls and slumps. We identified four sites (benches A–D) possessing ice-free surfaces, with minor evidence of post-deglacial transportation, which is required for proper application of exposure dates (e.g., jigsaw pattern of weathered bedrock and erratics on high-flat surfaces). We visited the David Glacier during 2017–2018 austral summer and focused on a vertical transect on Mt. Priestley.

The highest sampled landform, bench A (~1061 m asl), was dominated by highly weathered fragments of the underlying granite bedrock (Fig. 2B). The topmost ridge experienced negligible topographic shielding due to the surrounding cryoplanated surfaces, and it contained a small scoured U-shaped valley that flowed parallel to the David glacier. The second highest bench, bench B (~744 m asl) was more like a hill than a flat terrace (Fig. 2E); the bench surface was dominated by regolith. In contrast to the higher benches, no bedrock was visible on bench C (~545 m asl). Instead, the surface was thickly mantled with erratic boulders and cobbles of diverse lithologies (granite, quartzite, and volcanics), with granite being the most abundant rock found in the area (Fig. 2F). Similarly, Bench D (~222 m asl) was also covered with erratics, although these clasts were generally smaller in size (compared to those on bench C) (Fig. 2G). It is likely that the ice-free regions were sculpted by overriding ice from an inland ice sheet, rather than a local ice cap, because of the following observed features: (1) the distinctive peak summits compared to the nearby cryoplanated surfaces, (2) scoured U-shaped valleys flowing parallel and adjacent to the present David Glacier, and (3) various lithology of erratics supplied from different source areas.

3. Methodology

We employed paired-nuclide analysis (in-situ ^{26}Al & ^{10}Be) to determine the effective exposure ages of each bench. Cosmic rays produce cosmogenic nuclides in the atmosphere (meteoric) and lithosphere (in-situ) (Lal, 1991). Both isotopes are commonly produced in quartz and have half-lives long enough to cover the entire Quaternary period and beyond. ^{10}Be concentration was used to calculate the exposure ages of the bedrock and erratics, which were exposed and/or deposited following deglaciation. Previous studies indicate that comparison of the ^{26}Al/^{10}Be ratio in individual samples can be used to infer the exposure history and denudation rates of the rocks, due to the different half-lives of ^{26}Al and ^{10}Be (0.71 Ma and 1.38 Ma, respectively) (Lal, 1991; Gosse and Phillips, 2001). Lines of zero erosion and steady-state erosion bound

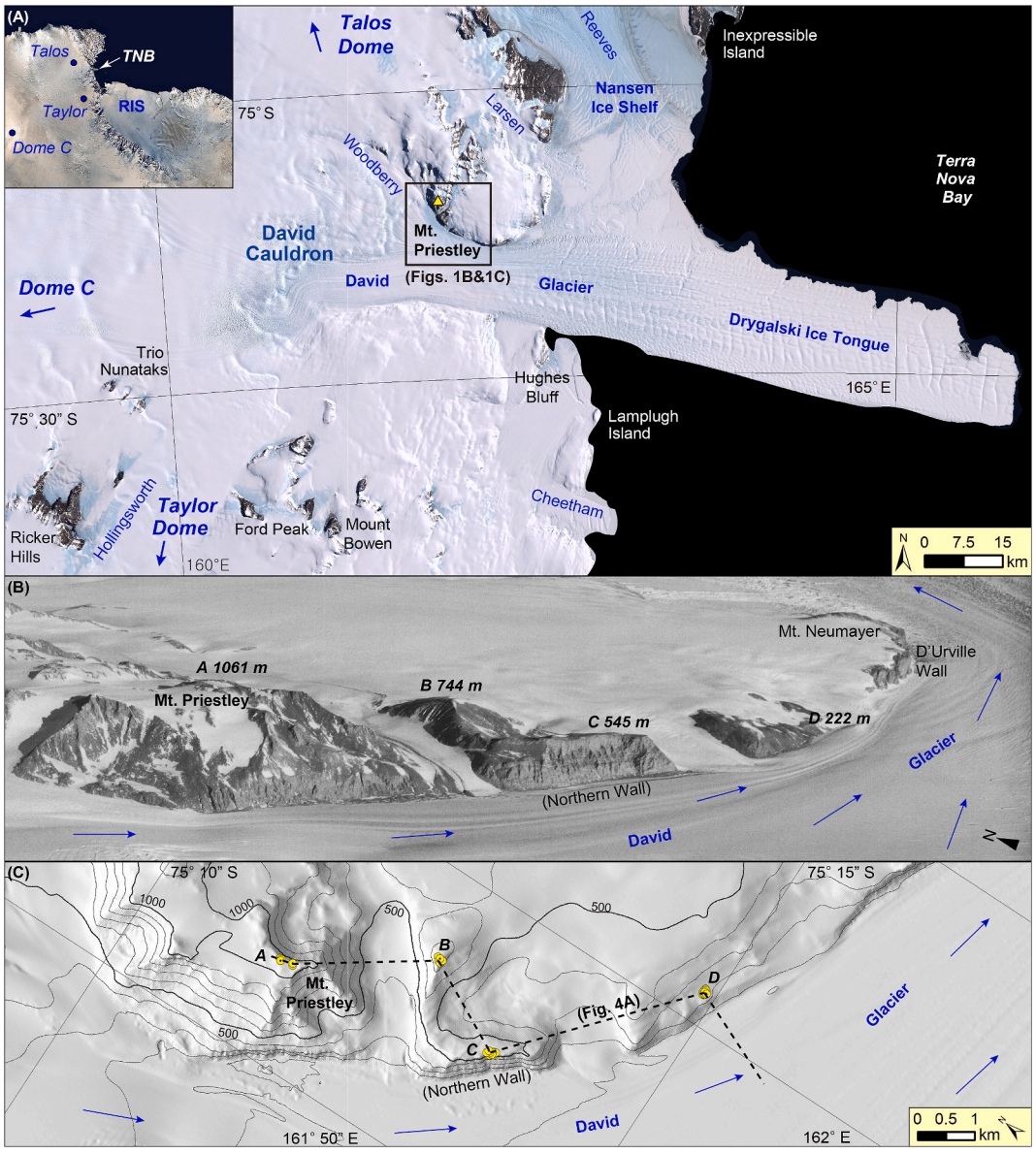

Fig. 1. Landsat Image Mosaic of Antarctica (LIMA) of the study area, which is the present terminal area of David Glacier. The white arrow in the index map indicates its location in Terra Nova Bay (TNB). David Glacier is fed by three major ice domes and drains into Terra Nova Bay and the western Ross Sea Embayment. (B) Aerial photo of the study area (Polar Geospatial Center, University of Minnesota). (C) Hill-shaded topographic map of the Mt. Priestley study area. Samples were collected from the four labeled benches (A, B, C, and D).

the zone of simple and continuous exposure, whereas lower isotopic ratios indicate a period of burial or rapid exhumation (Knudsen and Egholm, 2018). Therefore, we can determine whether a sample (from a bench) was continuously exposed, based on its positions on the two-isotope plot, with continuously exposed samples providing the closest estimates of the apparent exposure age. The resolution of the half-lives of ^{26}Al and ^{10}Be is suitable for resolving exposure ages older than ~200 ka (Lal, 1991; Gosse and Phillips, 2001), and it is also useful to evaluate simple exposure in younger samples (Lilly et al., 2010; Rhee et al., 2019, 2020).

Variable erosion rates with persistent ice burial might complicate the exposure/burial history, due to fluctuating ^{26}Al/^{10}Be ratios (Knudsen and Egholm, 2018); therefore, we aimed to collect samples only from non-fresh and paleo-glacially polished surfaces, where the removal of overriding ice has caused minor erosion (Fig. 2B). To minimize the impact of nuclide inheritance (Balco et al., 2013; Jeong et al., 2018; Rhee et al., 2020) or post-depositional reworking (Heyman et al., 2011; Rhee et al., 2019) on apparent exposure ages, we only sampled the isolated and gently sloping surfaces located away from high-angled slopes (e.g., cliffs, tors, and talus slopes) that could be disturbed by periglacial processes. Moreover, to statistically distinguish the probable outliers from erratics, we collected a larger number (n = 12) of samples from benches C and D than the higher benches (n = 5 from A and B).

We followed the physical and chemical treatment procedures outlined by the Korea University Geochronology Laboratory, Seoul, to extract and measure the in-situ ^{10}Be and ^{26}Al in the bedrock and erratic boulder samples (Kohl and Nishiizumi, 1992; Seong et al., 2016). Thirty-four samples were crushed, and fractions with grain sizes 250–500 μm were isolated for chemical treatment. The mineral grains from the granite samples were repeatedly leached in low-concentrated acids to remove other minerals and meteoric contaminants. A ^{9}Be carrier (983.6 ppm) was spiked and mixed with high-concentration HF and HNO_3 to dissolve the pure quartz grains. The ^{27}Al concentration of each sample aliquot (~5% of the total quartz amount) was measured at the

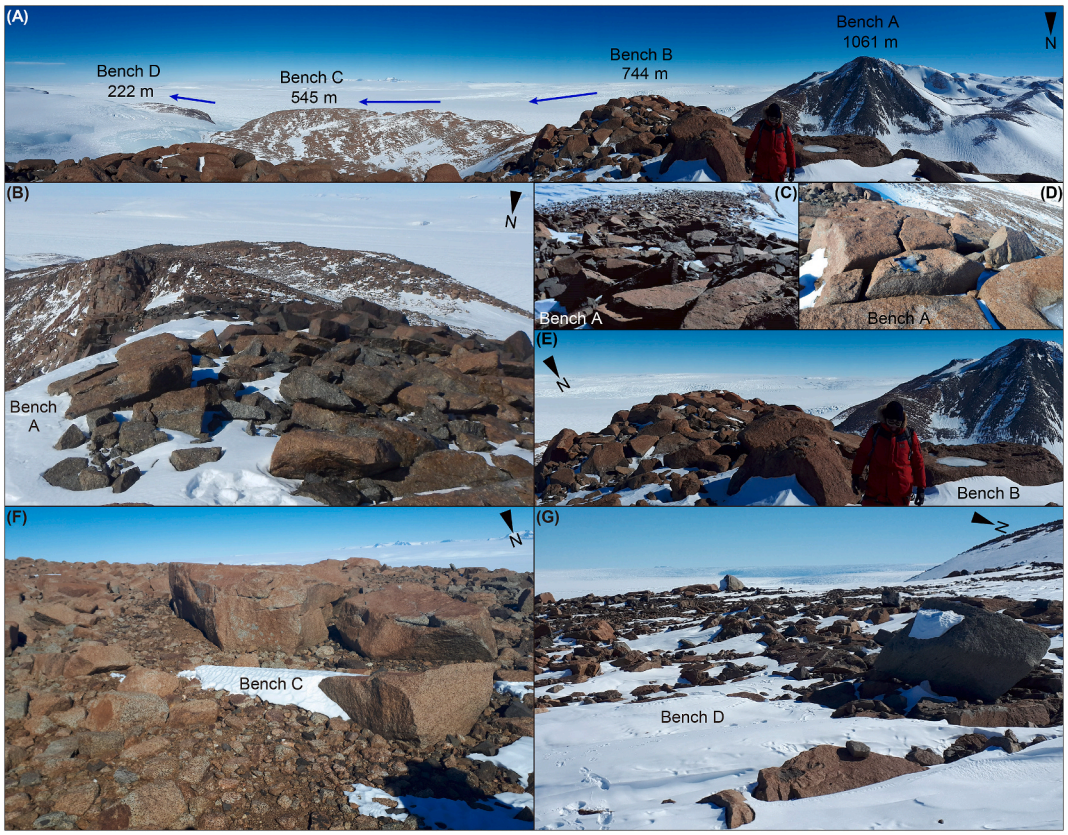

Fig. 2. (A) Panoramic view acquired from bench B. (B)–(D) Bench A. Granite bedrock samples were collected from the high-standing flat and polished surfaces, where post-depositional transportation and pre-depositional inheritance might not have occurred. The steep slopes beneath tors, cliffs, and cirques were excluded to avoid any samples that may have been supplied via slope processes. (E) Bench B also consists of weathered granite fragments that were well-preserved in situ due to limited transport processes. (F) Bench C covered with glacial erratics (granite, quartzite, volcanics). (G) Bench D, which is also covered with glacial erratics, although boulder-sized erratics are less common.

Korea Basic Science Institute, Seoul, using inductively coupled plasma-atomic emission spectroscopy (ICP-AES). We followed conventional chemical treatments with ion exchange columns and electric furnaces to prepare solid components for accelerator mass spectrometry (AMS) measurements, which were conducted at the Korea Institute of Science and Technology, Seoul.

The measured $^{10}Be/^{9}Be$ and $^{26}Al/^{27}Al$ ratios were normalized and converted to number of atoms after subtracting the process blanks. Subsequently, we calculated the exposure ages using version 3.0 of the CRONUS-Earth online exposure age calculator (Balco et al., 2008). The LSDn scaling factor (Lifton et al., 2014) and IceTEA tool were used for paired-nuclide analysis (Jones et al., 2019). All ages were calculated using 1σ errors (derived from AMS measurement), statistical counting of rare isotopes, standard-sample normalization, and blank correction. In case of the two-isotope ($^{26}Al/^{10}Be$) analysis, we winnowed simple exposure samples, of which 2σ ellipses overlapped the simple exposure zone, according to previous studies on Antarctica (Oberholzer et al., 2003, 2008; Di Nicola et al., 2009, 2012), while considering large error in ^{26}Al and the tolerance of the zone boundary (Balco, 2016, 2019).

4. Results

The apparent ^{10}Be exposure ages of the 34 samples span the last 1.5 Ma, and thus, correspond to the middle and late Pleistocene period (Table 1; Fig. 3A). Notably, the exposure ages of each bench generally decreased with declining elevation, and the four benches exhibited minor overlap in their exposure ages. The five bedrock fragments from areas surrounding the summit of Mt. Priestley (bench A; 1061 m asl) provided the oldest exposure age, with an apparent mean age of 1.13 ± 0.42 Ma. The five bedrock samples from bench B (744 m asl) had apparent exposure ages ranging from 0.3 to 0.8 Ma, with a mean age of 590.0 ± 181.4 ka. The ages of 12 erratic boulders sampled from bench C (545 m asl) ranged from 83.5 to 306.6 ka, with a mean age of 199.8 ± 64.7 ka. On bench D (222 m asl), 12 erratic samples showed exposure ages spanning the Last Glacial Period and the Holocene (85.0–1.8 ka), with an apparent mean age of 39.5 ± 30.9 ka.

In addition to ^{10}Be measurements, we also analyzed ^{26}Al in the bedrock and glacial erratic samples to establish whether the benches had undergone simple or complex exposure histories (Lal, 1991; Gosse and Phillips, 2001, Fig. 3B–E; Table 2). Old samples from the two bedrock benches (A: n = 4; B: n = 4) and clustered erratic samples from two benches covered by erratics (C: n = 6; D: n = 8) were chosen for the analysis. All four samples from bench A plotted inside the simple exposure zone showed $^{26}Al/^{10}Be$ ratio values of 4.6–5.1, with ages ranging from 1.1 to 1.4 Ma and a mean age of 1.31 ± 0.14 Ma. Only one significantly old sample from bench B (DVD010; 868.7 ± 65.4 ka) fell into the simple exposure zone having an isotope ratio of 5.4. The other three younger samples, despite of their highly clustered ages, had relatively lower isotope ratios (ranging from 5.1 to 5.2) and appeared to have been exposed multiple times (DVD 006–008; 527.2–615.2 ka).

All six samples from bench C (DVD 016–021), which were tightly clustered at ~250 ka also fell in the simple exposure zone, with a mean age of 234.2 ± 13.1 ka ($^{26}Al/^{10}Be$: 6.2–7.0). We selected eight samples from bench D, which predated the LGM (31.8–85.0 ka) for the two-isotope analysis and rejected the other four anomalously young samples from the Holocene (1.8–3.2 ka) as outliers, which reflects recent periglacial reworking. Five of the eight samples appeared to have undergone simple exposure during 50.3–85.0 ka (64.8 ± 13.7 ka), with

Table 1
Results of cosmogenic ^{10}Be analysis.

Name	Latitude (DD)	Longitude (DD)	Elevation (masl)	Thickness[a](cm)	Shielding Factor[b]	Quartz (g)	Be Carrier (g)[c]	Blank ^{10}Be Conc.[d,e](10^5 atoms)	^{10}Be/^{9}Be[e,f] (10^{-13})	^{10}Be Conc.[d,e](10^5 atoms·g^{-1})	Exposure Age[e,g] (ka)
Bench A (bedrock)											
DVD001	−75.18957	161.89425	1070.8	7	1.00000	49.82	0.4102	1.387 ± 0.580	252.585 ± 0.867	136.66 ± 1.45	1290 ± 108
DVD002	−75.18983	161.89427	1070.0	3.5	1.00000	49.75	0.4042	1.367 ± 0.571	237.375 ± 0.787	126.72 ± 1.34	1119 ± 89
DVD003	−75.18987	161.89325	1071.4	5.8	1.00000	45.29	0.3935	1.331 ± 0.556	95.863 ± 0.504	54.71 ± 0.62	417 ± 27
DVD004	−75.19183	161.89495	1044.6	4.6	1.00000	48.93	0.4203	1.421 ± 0.594	255.756 ± 0.816	144.36 ± 1.52	1401 ± 121
DVD005	−75.19169	161.89608	1048.9	3.2	1.00000	39.63	0.4105	1.388 ± 0.580	220.304 ± 0.741	149.96 ± 1.58	1449 ± 127
										[h]***Ave.***	**1135 ± 420**
Bench B (bedrock)											
DVD006	−75.21017	161.9481	741.0	3.7	0.99994	41.24	0.3991	1.349 ± 0.564	91.292 ± 0.617	58.03 ± 0.70	615 ± 43
DVD007	−75.21053	161.9465	747.0	2.5	0.99994	21.42	0.4193	1.418 ± 0.593	42.969 ± 0.339	55.22 ± 0.70	570 ± 39
DVD008	−75.21094	161.94575	745.7	4.9	0.99994	36.66	0.4059	1.372 ± 0.574	69.484 ± 0.425	50.52 ± 0.59	527 ± 36
DVD009	−75.21108	161.94757	736.1	4.3	0.99994	29.51	0.4109	1.389 ± 0.581	39.993 ± 0.385	36.55 ± 0.51	368 ± 24
DVD010	−75.21058	161.94786	749.1	3.5	0.99994	29.26	0.4063	1.374 ± 0.574	85.414 ± 0.496	77.91 ± 0.90	868 ± 65
										Ave.	**590 ± 181**
Bench C (erratics)											
DVD011	−75.22524	161.91556	537.5	2	0.99997	33.76	0.3933	1.330 ± 0.556	9.859 ± 0.178	7.51 ± 0.16	83.5 ± 5.3
DVD012	−75.22551	161.9158	537.7	5.2	0.99997	47.35	0.4165	1.408 ± 0.589	15.647 ± 0.305	9.02 ± 0.20	103.4 ± 6.7
DVD013	−75.22539	161.91491	522.2	4.5	0.99997	41.64	0.4171	1.410 ± 0.590	23.010 ± 0.311	15.12 ± 0.26	178 ± 11
DVD014	−75.22564	161.91773	554.2	4.4	0.99997	34.91	0.3989	1.349 ± 0.564	20.198 ± 0.272	15.13 ± 0.25	172 ± 11
DVD015	−75.22581	161.91715	554.1	9.3	0.99997	48.40	0.4361	1.475 ± 0.617	42.224 ± 0.575	24.97 ± 0.42	306 ± 20
DVD016	−75.22593	161.91699	549.4	9.7	0.99997	49.56	0.4212	1.424 ± 0.595	33.271 ± 0.481	18.55 ± 0.33	225 ± 14
DVD017	−75.226	161.91817	555.6	9.6	0.99997	48.05	0.4151	1.404 ± 0.587	33.926 ± 0.362	19.23 ± 0.28	232 ± 15
DVD018	−75.22558	161.91719	553.7	7.6	0.99997	33.20	0.3961	1.339 ± 0.560	26.438 ± 0.601	20.69 ± 0.52	246 ± 16
DVD019	−75.22565	161.91606	541.1	7.2	0.99997	50.06	0.3949	1.335 ± 0.558	40.652 ± 0.388	21.05 ± 0.29	253 ± 16
DVD020	−75.22521	161.91599	543.9	7.5	0.99997	41.88	0.3972	1.343 ± 0.562	30.101 ± 0.332	18.73 ± 0.28	224 ± 14
DVD021	−75.22481	161.91528	544.2	6.8	0.99997	44.81	0.4137	1.399 ± 0.585	30.930 ± 0.527	18.74 ± 0.37	222 ± 14
DVD022	−75.22499	161.91686	548.3	6.2	0.99997	49.13	0.4132	1.397 ± 0.584	23.142 ± 0.251	12.76 ± 0.19	147.8 ± 9.3
										Ave.	**199 ± 64**
Bench D (erratics)											
DVD025	−75.24832	162.01815	222.3	3.9	0.99933	15.67	0.4146	1.402 ± 0.586	2.710 ± 0.109	4.62 ± 0.20	70.7 ± 5.3
DVD026	−75.2484	162.02022	220.9	3.5	0.99933	23.45	0.4133	1.397 ± 0.584	2.915 ± 0.092	3.32 ± 0.11	50.3 ± 3.5
DVD027	−75.2481	162.02186	223.2	3.6	0.99933	48.11	0.4056	1.371 ± 0.573	7.992 ± 0.173	4.40 ± 0.11	67.0 ± 4.3
DVD028	−75.24806	162.02076	224.5	3.5	0.99933	49.56	0.4141	1.400 ± 0.585	8.180 ± 0.145	4.46 ± 0.09	67.8 ± 4.3
DVD029	−75.24801	162.0193	224.3	7.5	0.99933	47.48	0.4168	1.409 ± 0.589	3.597 ± 0.100	2.05 ± 0.06	31.8 ± 2.1
DVD030	−75.24816	162.01818	223.5	5.5	0.99933	49.97	0.4139	1.400 ± 0.585	0.450 ± 0.036	0.22 ± 0.02	3.2 ± 0.4
DVD031	−75.24838	162.01863	221.8	5	0.99933	29.89	0.4033	1.364 ± 0.570	6.243 ± 0.150	5.49 ± 0.15	85.0 ± 5.6
DVD032	−75.24845	162.01899	220.8	5.4	0.99933	44.94	0.4082	1.380 ± 0.577	5.900 ± 0.135	3.49 ± 0.09	53.9 ± 3.5
DVD033	−75.24837	162.02072	221.1	5.8	0.99933	52.33	0.3949	1.335 ± 0.558	0.461 ± 0.036	0.20 ± 0.02	3.0 ± 0.4
DVD034	−75.24825	162.02135	221.4	7.8	0.99933	46.25	0.3959	1.339 ± 0.560	0.260 ± 0.029	0.12 ± 0.02	1.8 ± 0.3

(*continued on next page*)

Table 1 (*continued*)

Name	Latitude (DD)	Longitude (DD)	Elevation (masl)	Thickness[a](cm)	Shielding Factor[b]	Quartz (g)	Be Carrier (g)[c]	Blank ^{10}Be Conc.[d,e](10^5 atoms)	^{10}Be/^{9}Be[e,f] (10^{-13})	^{10}Be Conc.[d,e](10^5 atoms·g^{-1})	Exposure Age[e,g] (ka)
DVD035	−75.24827	162.02012	222.2	6.5	0.99933	40.00	0.4026	1.361 ± 0.569	3.751 ± 0.231	2.45 ± 0.16	37.9 ± 3.3
DVD036	−75.24864	162.01957	218.9	6.5	0.99933	50.47	0.4132	1.397 ± 0.584	0.287 ± 0.028	0.13 ± 0.02	1.9 ± 0.3
										Ave.	**39 ± 30**

[a] Thickness of samples (granite bedrock and erratics; density: 2.7 g cm^{-3}).
[b] Factors for correcting geometric shielding measured on intervals of 10°.
[c] 983.56 ppm of ^{9}Be carrier was used.
[d] A mean value of process blank samples (5.144 × 10ˆ-15 ± 2.150 × 10ˆ-15) was used for correction of background.
[e] Uncertainties are calculated at the 1σ confidence level.
[f] Ratios of ^{10}Be/^{9}Be were normalized with 07KNSTD reference sample 5–1 (2.709 × 10ˆ-11 ± 8.824 × 10ˆ-14) of Nishiizumi et al. (2007) and ^{10}Be half-life of 1.38 × 10ˆ6 (Korschinek et al., 2010).
[g] Ages are calculated assuming zero erosion with using CRONUS-Earth online calculator 3.0 (Balco et al., 2008) with scaling factors of LSDn (Lifton et al., 2014).
[h] Apparent mean ages on each bench.

relatively large 1σ error, compared to other benches and isotopes ratios of 6.4–7.3. One of the three multiple exposed samples (DVD 025; 70.7 ka) was also included in the age range of other simply exposed samples; however, its ^{26}Al concentration was abnormally low due to the relatively high ^{27}Al concentration (^{26}Al/^{10}Be: 1.4; Table 2). We speculate that these outliers were either previously exposed or more recently shattered and eroded to yield the older and younger ages, respectively (Heyman et al., 2011). The other two samples at ~30 ka (DVD 029 and 035) plotted on the multiple exposure zone, with relatively low isotope ratios (5.4 & 6.3).

The bedrock surfaces of the two highest benches have been extensively weathered since deglaciation such that they now exhibit a mantle of shattered bedrock fragments, well-developed pits, and disintegrated tors. Therefore, we corrected the simple exposure ages for probable surface erosion using their own denudation rates (Table 3; ~16 cm/Ma). The simple and continuously exposed bedrock surfaces on bench A were corrected to provide ages of 1.47–2.18 Ma, with a mean of 1.77 ± 0.32 Ma. This time period corresponds to the early Pleistocene (Fig. 3F). The simply exposed surface on bench B was also corrected from 868.7 ± 65.4 ka to 1.30 ± 0.17 Ma (Table 3).

5. Discussion

5.1. Chronological changes in ice thickness on Mt. Priestley

We used the erosion-corrected bedrock ages (benches A and B) and simple exposed erratic ages (benches C and D), in conjunction with the ^{26}Al–^{10}Be two-isotope analyses, to reconstruct the glacial history of the four benches. The multiple exposed samples were most likely influenced by post-deglacial reworking and/or recent exposure by exfoliation, which might underestimate the actual deglaciation period. Our data suggest that the summit of Mt. Priestley (~1071 m asl) was exposed at 1.77 ± 0.32 Ma (MIS 63), around the early Pleistocene (Fig. 4A), and has remained ice-free since then. If this is true, the pattern implies that the David Glacier was thicker during the Pliocene than the Pleistocene and has not readvanced over Mt. Priestley since the early Pleistocene. Moreover, this scenario indicates that the surface of David Glacier dropped below 736 m asl by 1.30 ± 0.17 Ma, suggesting a low apparent thinning rate (0.67 m/kyr; MIS 63–41; Fig. 4A) through repeated glacial and interglacial periods of thickening and thinning, respectively.

The maximum ice surface elevation continued to decrease during the Middle Pleistocene, which dropped to <545 m asl by 234.2 ± 13.1 ka (MIS 7). This formed the longest period in glacier lowering when the apparent thinning rate was the lowest (~1 Myr; 0.18 m/kyr; Fig. 4A). Simple exposures of the elevated surfaces indicate that David Glacier was thicker during the previous MIS 8 glaciation and thinner during MIS 6 and MIS 2–4 (Fig. 4B). We suggest that this degree of thinning marks the maximum limit of either MIS 6 or MIS 4 (Fig. 4C). This long-term pattern of Quaternary down-wasting agrees well with changes in the Taylor and Ferrar glaciers in the Southern Victoria Land, where stepwise ice recession has left moraine/drifts since the mid-Pliocene (Staiger et al., 2006; Swanger et al., 2011). The adjacent regions of Hatherton Glacier exhibited a pattern of decreasing ice volume on its drifts over the last 2 Ma, along with as decreasing ice volume on the Law Glacier during the mid-late Pleistocene (Joy et al., 2014; Kaplan et al., 2017). This implies that the volume of East Antarctic Ice Sheet was apparently reduced on the outlet glaciers of the Ross Embayment during the Quaternary period.

The surface of David Glacier has remained lower than 222 m asl since 64.8 ± 13.7 ka (mid MIS 4). Moreover, our calculations indicated that the apparent thinning rate between benches C and D increased rapidly to 1.90 m/kyr (234.2–64.8 ka; Fig. 4A). We speculate that the local LGM (MIS 4) preceded the LGM (MIS 2) at >222 m asl, implying that the ice surface during MIS 2 might have reached elevations of only <222 m asl. If this is true, bench D marks the minimum ice limit of either MIS 6 or MIS 4, and it also constitutes the maximum ice limit for MIS 2. Two major trimlines (T1 and T2) occurred on the northern wall of the David Glacier between the exposed MIS 7 and MIS 4 levels (Fig. 4D), indicating that the glacier either minorly fluctuated or continuously thinned between these two periods. Following the local LGM during MIS 4, the ice surface remained lower than 222 m, even during MIS 2. Finally, thinning of the David Glacier during the post-LGM and Holocene (MIS 1) periods at an extremely fast rate of 2.34 m/kyr brought the ice surface to ~70 m asl.

5.2. Ice dynamics in Terra Nova Bay

Previous studies on cosmogenic exposure dating reveal that the ice-free regions alongside the outlet glaciers draining into Terra Nova Bay have experienced continuous exposure at million-year timescales (Fig. 5A; Oberholzer et al., 2003, 2008; Di Nicola et al., 2009, 2012; Strasky et al., 2009). Specifically, these studies reported that the transition from warm to cold-based glaciation occurred prior to the timing of initial exposure, during 1.2–6.0 Ma, when the long-term denudation rates were extremely low. The highest magnitude of lowering occurred at i) Mt. Pollock, which was initially exposed at ~6 Ma and had lost 800 m of ice along Campbell Glacier, and ii) Archambault Ridge, which experienced 600 m of ice lowering over a similar time period (Di Nicola et al., 2012). Since 3.8 ± 0.5 Ma, Mt. Abbott also experienced extensive lowering (770 m) of ice surface at the Browning Pass, which lies between the Campbell and Priestley glaciers (Di Nicola et al., 2009). The neighboring Mt. Keinath underwent a similar magnitude of lowering (600 m) since 3.8 ± 0.6 Ma (Oberholzer et al., 2003).

We note that the magnitude of thinning was greater along the

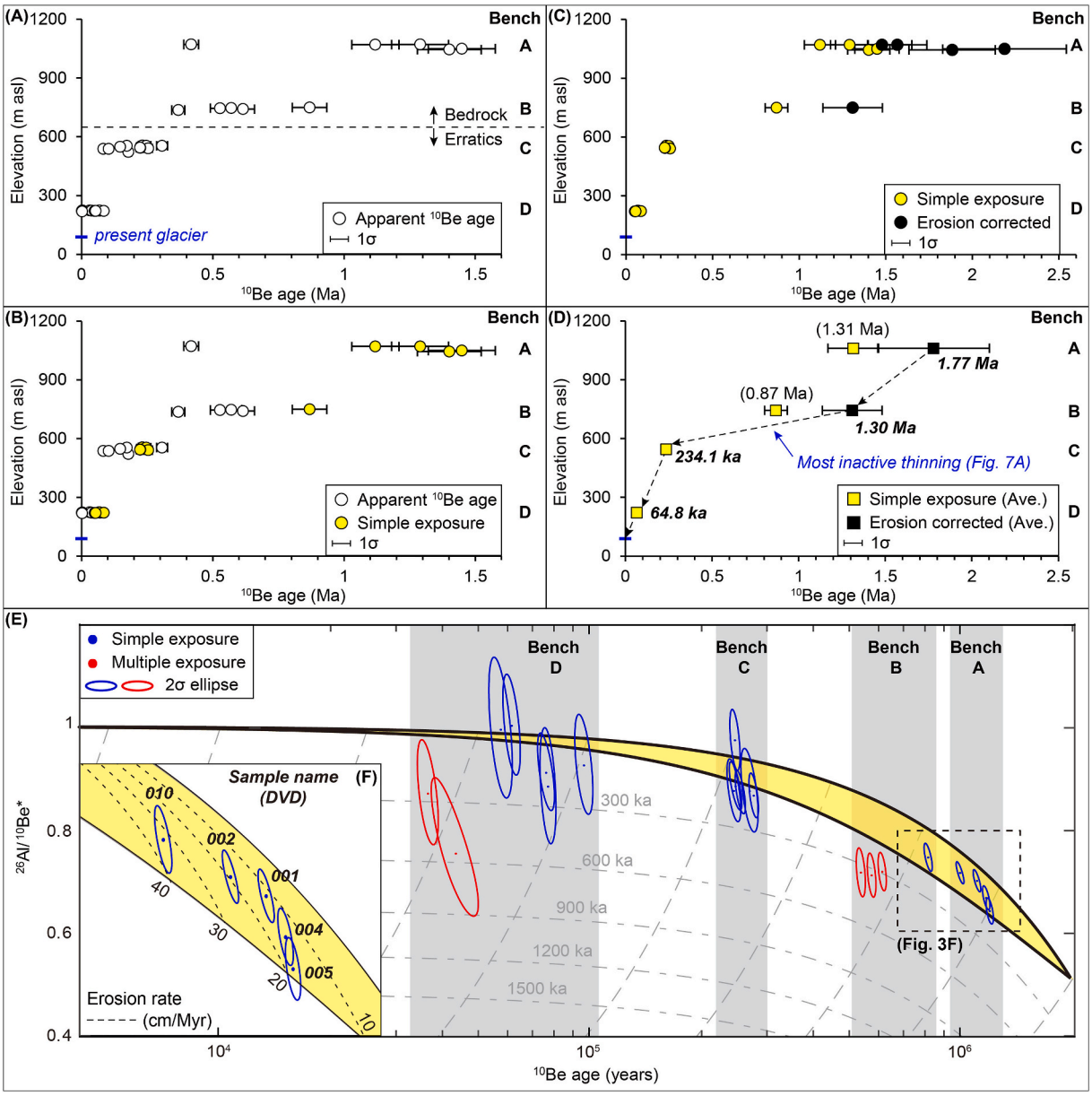

Fig. 3. (A) Apparent ^{10}Be ages (white circles) of the four benches on Mt. Priestley (Table 1). (B) Simple exposures (yellow circles) among the samples based on the ^{26}Al/^{10}Be analysis (Fig. 3E & Table 2). (C) Simple exposures and erosion-corrected results of bedrock samples (black circles). (D) Arithmetic mean ages (rectangles) of each bench. (E) Two-isotope plot (^{10}Be and ^{26}Al) and erosion rate curves of samples using IceTEA tool (modified from Jones et al., 2019). The blue ellipses are the 2σ error ranges which fall into the yellow sections (simple exposure zone), while red ellipses experienced burial history (Tables 2 and 3). (F) Simply exposed bedrock samples on bench A (n = 4) and B (n = 1) were corrected with their own erosion rate (Table 3).

northern glaciers in the Terra Nova Bay than the southern outlet glaciers (Fig. 5A). The maximum thinning in the southern region occurred along the Hollingsworth Glacier, a tributary glacier of David Glacier, whose surface has dropped by 500 m since the exposure of the Ricker hills 1.2 Ma (Fig. 5B; Strasky et al., 2009). Small north-flowing glaciers in the vicinity also experienced 200–300 m of surface lowering at Ford Peak and Mt. Bowen (uncorrected ^{21}Ne ages; Oberholzer et al., 2008). In addition to quantifying the patterns of glacier thinning, our results also suggested that the David Glacier was a cold-based glacier on Mt. Priestley (at 1.77 ± 0.32 Ma) and had an elevation of ~1071 m asl. Notably, the glacier has preserved the eroded bedrocks, similar to the previously studied sites in Victoria Land (Oberholzer et al., 2003; Di Nicola et al., 2009; Strasky et al., 2009). Given the published and present data, the highest magnitude of Quaternary thinning (~990 m) might have occurred in the lower reaches of David Glacier, where the ice surface lowering was greater than any other outlet glaciers draining into the Terra Nova Bay.

The maximum duration of exposure of the high-elevation surfaces at Ricker Hills (1455–1589 m asl; 1.25 ± 0.17 Ma; Strasky et al., 2009) is similar to our results from bench B (744 m asl; 1.30 ± 0.17 Ma). Moreover, the magnitude of thinning since the middle Pleistocene was also similar at both the sites (i.e., Ricker Hills at ~500 m and Mt. Priestley at ~665 m) (Fig. 5B). Although the low-elevation surfaces at Ricker Hills provide exposure ages (230 ± 7 ka and 69 ± 2 ka; Strasky et al., 2009) that are close to our ages from benches C and D at Mt. Priestley (234.2 ± 13.1 ka and 64.8 ± 13.7 ka), the two sites underwent different degrees of lowering. At Ricker Hills, for instance, surface lowering occurred over a much narrower elevation zone (1435–1438 m asl), compared to that at Mt. Priestley (222–545 m asl), which suggest that, during the late Pleistocene, Mt. Priestley has experienced more

Table 2
Result of ^{10}Be and ^{26}Al analysis.

Name	Elevation (masl)	Al			Be			^{26}Al/^{10}Be[g]
		^{26}Al/^{27}Al[a,b] (10^{-12})	^{27}Al conc.[c,b] (10^{18} atoms g^{-1})	^{26}Al conc.[b] (10^{6} atoms g^{-1})	^{10}Be/^{9}Be[d,b] (10^{-13})	^{10}Be conc.[b] (10^{5} atoms g^{-1})	^{10}Be exposure age[e,f,b] (ka)	
Bench A								
DVD001	1070.8	69.941 ± 0.601	0.98 ± 0.01	69.22 ± 0.59	252.585 ± 0.867	136.66 ± 1.45	*1290 ± 108*	***5.06 ± 0.13***
DVD002	1070.0	73.630 ± 0.578	0.89 ± 0.00	65.59 ± 0.51	237.375 ± 0.787	126.72 ± 1.34	*1119 ± 89*	***5.17 ± 0.13***
DVD004	1044.6	57.642 ± 0.688	1.20 ± 0.02	69.69 ± 0.83	255.756 ± 0.816	144.36 ± 1.52	*1401 ± 121*	***4.82 ± 0.15***
DVD005	1048.9	54.443 ± 0.821	1.27 ± 0.01	69.59 ± 1.04	220.304 ± 0.741	149.96 ± 1.58	*1449 ± 127*	***4.64 ± 0.17***
						Ave.	**1315 ± 146**	
Bench B								
DVD006	741.0	12.353 ± 0.265	2.44 ± 0.02	30.23 ± 0.64	91.292 ± 0.617	58.03 ± 0.70	615 ± 43	5.21 ± 0.25
DVD007	747.0	10.525 ± 0.270	2.70 ± 0.04	28.49 ± 0.73	42.969 ± 0.339	55.22 ± 0.70	570 ± 39	5.15 ± 0.29
DVD008	745.7	11.277 ± 0.281	2.32 ± 0.01	26.26 ± 0.65	69.484 ± 0.425	50.52 ± 0.59	527 ± 36	5.19 ± 0.28
DVD010	749.1	14.899 ± 0.177	2.82 ± 0.09	42.16 ± 0.50	85.413 ± 0.496	77.91 ± 0.90	*868 ± 65*	***5.41 ± 0.17***
						Ave.	**868 ± 65**	
Bench C								
DVD016	549.4	7.598 ± 0.122	1.56 ± 0.03	11.92 ± 0.19	33.270 ± 0.481	18.55 ± 0.32	*225 ± 14*	***6.42 ± 0.30***
DVD017	555.6	7.599 ± 0.125	1.60 ± 0.03	12.19 ± 0.20	33.925 ± 0.361	19.23 ± 0.28	*232 ± 15*	***6.34 ± 0.28***
DVD018	553.7	4.581 ± 0.163	2.87 ± 0.08	13.15 ± 0.46	26.437 ± 0.600	20.69 ± 0.51	*246 ± 16*	***6.35 ± 0.55***
DVD019	541.1	7.412 ± 0.138	1.78 ± 0.03	13.25 ± 0.24	40.652 ± 0.388	21.05 ± 0.29	*253 ± 16*	***6.29 ± 0.29***
DVD020	543.9	3.651 ± 0.089	3.63 ± 0.08	13.26 ± 0.32	30.100 ± 0.332	18.73 ± 0.27	*224 ± 14*	***7.07 ± 0.40***
DVD021	544.2	3.379 ± 0.086	3.52 ± 0.07	11.92 ± 0.30	30.929 ± 0.526	18.73 ± 0.37	*222 ± 14*	***6.36 ± 0.41***
						Ave.	**234 ± 13**	
Bench D								
DVD025	222.3	0.014 ± 0.002	44.8 ± 2.86	0.67 ± 0.10	2.710 ± 0.109	4.62 ± 0.19	70.7 ± 5.3	1.45 ± 0.39
DVD026	220.9	0.124 ± 0.006	19.2 ± 0.82	2.40 ± 0.13	2.914 ± 0.091	3.31 ± 0.11	*50.3 ± 3.5*	***7.25 ± 0.92***
DVD027	223.2	2.831 ± 0.083	1.03 ± 0.02	2.92 ± 0.08	7.992 ± 0.173	4.40 ± 0.10	*67.0 ± 4.3*	***6.64 ± 0.50***
DVD028	224.5	0.978 ± 0.048	2.94 ± 0.05	2.87 ± 0.14	8.179 ± 0.145	4.46 ± 0.09	*67.8 ± 4.3*	***6.44 ± 0.68***
DVD029	224.3	0.918 ± 0.042	1.41 ± 0.02	1.29 ± 0.05	3.596 ± 0.099	2.04 ± 0.06	31.8 ± 2.1	6.34 ± 0.69
DVD031	221.8	1.104 ± 0.046	3.35 ± 0.11	3.70 ± 0.15	6.242 ± 0.149	5.49 ± 0.14	*85.0 ± 5.6*	***6.74 ± 0.66***
DVD032	220.8	1.408 ± 0.053	1.81 ± 0.04	2.55 ± 0.09	5.900 ± 0.134	3.49 ± 0.08	*53.9 ± 3.5*	***7.30 ± 0.67***
DVD035	222.2	1.364 ± 0.059	0.98 ± 0.02	1.34 ± 0.05	3.751 ± 0.230	2.44 ± 0.15	37.9 ± 3.3	5.49 ± 0.84
						Ave.	**64 ± 13**	

[a] Ratios of ^{26}Al/^{27}Al were normalized with KNSTD reference sample 4–1 (7.444 × 10^-11 ± 1.011 × 10^-12) of Nishiizumi et al. (2007).
[b] Uncertainties were calculated at the 1σ confidence level.
[c] Concentration of ^{27}Al was measured with ICP-AES from quartz dissolution aliquot.
[d] Ratios of ^{10}Be/^{9}Be were normalized with 07KNSTD reference sample 5–1 (2.709 × 10^-11 ± 8.824 × 10^-14) of Nishiizumi et al. (2007) and ^{10}Be half-life of 1.38 × 10^6 (Korschinek et al., 2010).
[e] Ages are calculated assuming zero erosion with using CRONUS-Earth online calculator 3.0 (Balco et al., 2008) with scaling factors of LSDn (Lifton et al., 2014).
[f] Italic values are ages of simple exposed samples (Fig. 3B and E) and bold values are mean of them.
[g] ^{26}Al/^{10}Be ratio and 2σ error range of each sample was checked for finding simple exposure (bold italic) with two-isotope plot using IceTEA tool on Fig. 3E (Jones et al., 2019).

rapid lowering than Ricker Hills.

Cosmogenic dating of the Jangbogo Hills at the terminal regions of the Campbell Glacier suggests that the local LGM occurred prior to 35.4 ± 2.4 ka, when the ice surface was 100–150 m above the present level (Rhee et al., 2019). Subsequently, the Campbell Glacier experience ice cover reduction during 35.4 to 17.0 ka, which led the glacier surface to stand at <100 m above its present-day level. The simple exposed erratics (50 ka) on the Grove Mountains in the interior EAIS also indicate the prevalence of thicker and more extensive ice prior to the LGM (Lilly et al., 2010). Both arguments on the interior and terminal sides of the EAIS indicate that the local LGM preceded the global LGM. These results are supported by our expanded results in vertical cross-section, which experienced the most dramatic thinning during the Quaternary (Fig. 5B). Other cosmogenic dating studies have described similar patterns of post-LGM deglaciation along the Victoria Land outlet glaciers, where the surfaces of Mackay, Priestley, Tucker, and Aviator glaciers decreased by as much as ~300 m during the post-LGM period (Jones et al., 2015; Goehring et al., 2019; Rhee et al., 2020). Our results suggest that ice thickness (that decreased prior to the LGM) and thinning trend continued into the post-LGM period.

5.3. Glacier dynamics driven by climatic changes

To reconstruct the glacial history of David Glacier, we compared our

Table 3
Erosion-corrected ages of bench A and B.

Name	Elevation (masl)	^{10}Be exposure age[a] (ka)	Erosion correction	
			ε (cm/Myr)[b]	Corrected age[c] (ka)
Bench A				
DVD001	1070.8	1290 ± 108	12	1566 ± 171
DVD002	1070.0	1119 ± 89	19	1478 ± 172
DVD004	1044.6	1401 ± 121	15	1883 ± 249
DVD005	1048.9	1449 ± 127	18	2185 ± 357
	Ave.	1315 ± 146	16	1778 ± 322
Bench B				
DVD010	749.1	868 ± 65	34	1308 ± 172

[a] ^{10}Be exposure ages of simple exposed bedrock samples (Tables 1 and 2).
[b] Erosion rate was calculated with the IceTEA tool (modified from Jones et al., 2019).
[c] Ages were recalculated with erosion rates using CRONUS-Earth online calculator 3.0 (Balco et al., 2008) and scaling factor of LSDn (Lifton et al., 2014).

deglacial records with paleoclimate proxies during the Pleistocene, which reflect the conditions of ice accumulation or ablation (Figs. 6 and 7). The surface temperature and ice accumulation rates on Dome C, and the authigenic ^{10}Be concentrations in the Southern Ocean may contain the record of climatic changes in the David Glacier, which is located between Dome C and the Southern Ocean (Jouzel et al., 2007; Parrenin et al., 2007; Dash et al., 2021). The longest authigenic ^{10}Be records, which span the last ~1 Ma (RS15-LC42; 1175 cm), represent the reconstructed climatic history based on the persistent sea ice on the outermost boundary of Antarctica (margin of the Ross Sea continental shelf). Magnetic polarity of this core exhibited normal-to-reverse magnetism at 8.26 ± 0.03 m (0.781 Ma), which is a key stratigraphic marker horizon for chronological constraints (Ohneiser et al., 2019). The age of the core was determined based on the assumption of a constant sediment rate (Ohneiser et al., 2019), and the ^{10}Be concentration and ^{10}Be/^{9}Be ratio were decay-corrected based on age (Dash et al., 2021).

We divided the Pleistocene into three periods, based on the Milankovitch cycle shift (41–100 kyr cycles) dominant during the middle Pleistocene transition (MPT and pre & post-MPT), which caused the insolation change (Snyder, 2016). The temperature continued to decrease throughout the Pleistocene; however, the increasing amplitude of temperature resulted in warm interglacial events. We roughly marked the warmer interglacials period during the Pleistocene, which have similar trends of lowering dominant exposure age data and vice versa (Fig. 7A). Then, we sub-divided the post-MPT into two periods when the insolation-induced climatic transition occurred with extreme interglacial periods (mid-Brunhes transition event (MBE); pre- & post-MBE; Yin, 2013). The temperature was maintained to show an overall decreasing pattern; however, the fluctuations between the glacial and interglacial periods were amplified toward warmer interglacial periods, which agree with our deglaciation records during post-MBE (Fig. 7B). The periods indicated by colored boxes are based on authigenic ^{10}Be concentrations, related to the persistence of sea ice (10^8 atoms/g; Figs. 7B–6).

We summarize that thicker ice existed before Pleistocene, and the ice continued to decrease until it reached the summit of Mt. Priestley during the early Pleistocene. The first exposure to cosmogenic nuclides in the summit of Mt. Priestley occurred at 1.77 ± 0.32 Ma (1.47–2.18 Ma), which covered almost the entire pre-MPT. The temperature during this period was generally warmer than the subsequent periods with little temperature fluctuation between glacial and interglacial periods under the dominancy of a short 41-kyr obliquity cycle, which caused the overall lowering of the glacier (Fig. 7A; Snyder, 2016). However, temperature fluctuation became more amplified toward colder conditions during the second half of pre-MPT, causing glaciers to be show minimal lowering due to lower ablation for ~0.5 Myr until the next exposure (constrained by bedrock bench B) occurring at 1.30 ± 0.17 Ma. The temperature fluctuations increased leading to colder glacial periods, with decreased δ^{18}O values of planktonic and benthic forms during the late pre-MPT and MPT (1.38–0.9 Ma; Thissen et al., 2003); however, this resulted in l warmer interglacial conditions. Ice lowering was the most dominant factor that caused the reduction of Antarctic Ice Sheet volume, along with high ablation and relatively low accumulation, which probably occurred due to the cold and arid polar climate during glacial periods.

MPT (1.2–0.9 Ma) experienced the Milankovitch cycle shift from low-amplitude and high-frequency 41-kyr to high-amplitude and low-frequency 100-kyr cycles, causing colder conditions post-MPT (Snyder, 2016). The high-amplitude condition caused greater magnitude of ice configurations during the glacial/interglacial periods on the EAIS; however, David glaciers have maintained similar patterns in its vertical and horizontal extent, with minor unbalanced lowering during advancing and thickening during retreating (Sutter et al., 2019).

The pre-MBE (0.8–0.43 Ma) period experienced declining temperatures (Figs. 7B–1), which not only caused the ice sheet in the Northern hemisphere to grow (Thissen et al., 2003; Snyder, 2016) but also generated strong Antarctic bottom water formation with a cooler deep ocean (Yin, 2013). Temperature deviations in the interior EAIS (Dome C: EDC3; Jouzel et al., 2007) decreased with limited temperature variations (Figs. 7B–2). The declining air temperatures reduced the net precipitation, resulting in lower accumulation at Dome C (Parrenin et al., 2007, Figs. 7B–3). Authigenic ^{10}Be concentrations were also depleted due to the increase in the thick permanent sea ice cover, except for a small seasonal sea ice open period between 0.8 and 0.7 Ma (MIS 19–17; Figs. 7B–4 and 5). The pre-MBE was a cold and arid period, during which glaciers underwent minimal lowering. Ice modeling suggest that the ice volume had increased by ~30% during post-MPT, compared to the MPT and pre-MPT periods, in the latter case the ice thickness varied by only ~5% (Sutter et al., 2019). This corresponds well with our simple exposure dates of benches A and B that exhibit negligible overriding expansion, while the ice on the Ross Sea varied considerably in the horizontal direction.

The post-MBE (0.43 Ma to present) period experienced warmer interglacial periods (yellow sections in Fig. 7B) such that the sea ice cover in the Central Basin almost disappeared seasonally. The high authigenic ^{10}Be periods in our record correspond well with the post-MBE interglacial periods (MIS 1, 5, 9, and 11), which were warmer than the pre-MBE interglacial periods (MIS 13, 15, and 17). The temperature difference at EDC3 also exceeded the present level during these interglacial periods, reaching higher values than during the pre-MBE (Figs. 7B–3). These warm interglacial conditions occurred when the Antarctic air temperature was higher than that at present, with decreased iceberg-rafted debris from ice margins and ice volume reduction in Antarctica (Wilson et al., 2018). These extreme warm peaks coincided with rapid increase in the thinning rate of the David Glacier from bench C to bench D, and subsequently, to its present level. It also matches well with the low-exposed surfaces on the Ricker Hills during the end of the Pleistocene (Figs. 4A and 5). The low authigenic ^{10}Be also corresponds well with the glacial periods (MIS 10, 8, and 6), except for the Last Glacial period (MIS 4 and 2). The Central Basin was finally covered with permanent thick sea ice during the Penultimate Glacial Maximum (PGM) during MIS 6 and has completely transited to seasonal open sea ice since then, demonstrated by the continuous increment of authigenic ^{10}Be concentration. The sea ice coverage corresponds well with our terrestrial lowering dominant data, indicating that the glacier level was greater during the PGM than the local LGM and LGM.

We suggest that the lowering of dominant glacial histories through the Pleistocene was primarily driven by climate change, particularly through the warm peak periods (pre-MPT and post-MBE; Fig. 7A). Modeling of Antarctic ice volume and thickness changes by climate forcing transition agree well with our terrestrial deglaciation phases. Ice thickening was poor during glacial periods, even in the center of the dome (accumulation zone) due to the hyper-arid low accumulation

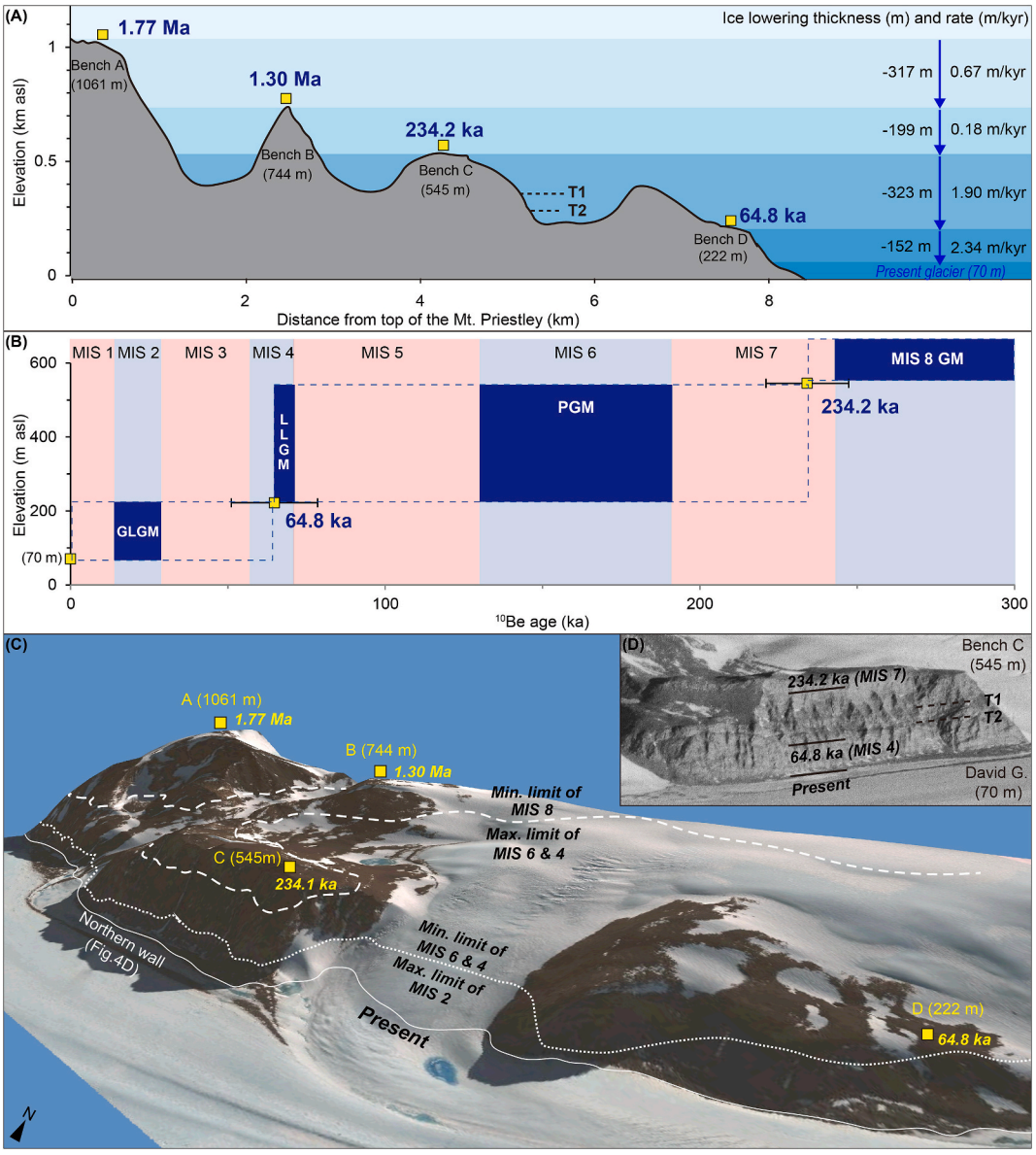

Fig. 4. (A) Longitudinal profile of the study area and exposure ages (yellow squares) during deglaciation of David Glacier. The apparent thinning rates are determined by dividing the elevation of each exposed bench by its age. (B) Exposure age and elevation changes over the last 300 ka. The boxes with dashed lines represent the age and elevation ranges based on our age dating results (yellow squares). The dark-blue boxes are the potential spatiotemporal ranges of each glacial maximum (GM: Glacial Maximum; PGM: Penultimate Glacial Maximum; LLGM: Local Last Glacial Maximum; GLGM: Global Last Glacial Maximum) (C) 3D image with some upper limits of the David Glacier that were constrained by our study for the late Quaternary. The dashed line is the minimum limit of MIS 8 and maximum limit of MIS 6 and 4. The dotted line is the minimum limit of MIS 6 & 4, and the maximum limit of MIS 2. (D) Two major trimlines (T1 and T2) are found on the northern wall of David Glacier, between the glacier limits of MIS 7 and 4 (Oblique Aerial photo from Polar Geospatial Center, University of Minnesota).

(Fig. 7B). Even in the cold post-MPT, the accelerated thinning rate of the David Glacier during late Pleistocene corresponds well with the relatively warm periods (MIS 11–1; post-MBE), compared to the slight lowering observed during the cold periods (MIS 22–12; pre-MBE). Additional modeling on climatic and sea level dynamics can provide a more detailed understanding of ice dynamics throughout the Quaternary, the minor records of which cannot be provided by cosmogenic exposure dating studies.

6. Conclusions

David Glacier is one of the largest outlet glaciers draining the EAIS into the Ross Sea Embayment, and it possesses the largest ice drainage area and the fastest ice-flow velocity in Victoria Land. It is widely accepted that the most dynamic deglaciation of Mt. Priestley occurred within the current terminus zone of the glacier. Using our newly obtained terrestrial cosmogenic ages and the published marine authigenic isotope data, in this study, we demonstrated that the Quaternary history of the David Glacier was dominated by monotonic lowering. Such monotonic lowering dominated the David Glacier on the Terra Nova Bay of central Victoria Land, which corresponds well with previous reports on stepwise ice lowering over the Southern and Northern Victoria Land. The compiled simple or constant exposures revealed by paired cosmogenic nuclide exposure data support that the EAIS margin along the western Ross Sea experienced a dominant ice-wasting throughout the Pleistocene and/or since the Pliocene.

The bedrock benches A and B were exposed at 1.77 ± 0.32 Ma and 1.30 ± 0.17 Ma, respectively, with no overriding glacier advances or thickening since the early Pleistocene. David Glacier has been characterized by cold-based conditions since 1.77 Ma, with these upper two

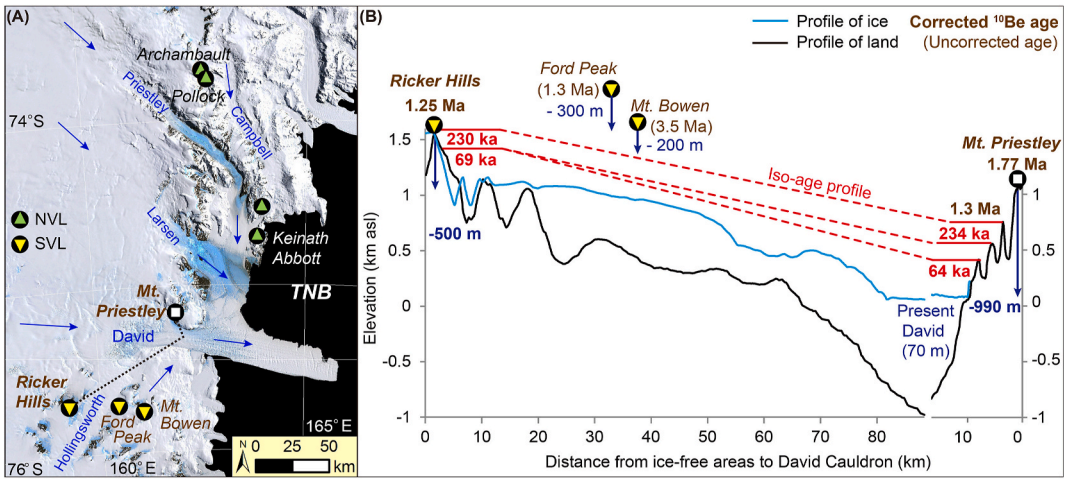

Fig. 5. (A) Locations of the previously studied areas that employed cosmogenic nuclide dating in Terra Nova Bay. The yellow squares denote the locations of ice-free areas in the northern local valley glaciers (Archambault Ridge; Mt. Pollock; Mt. Keinath; Mt. Abbott). Green squares indicate southern dome-derived ice sheet glaciers (Ricker Hills, Ford Peak, Mt. Bowen), respectively. (B) Longitudinal profiles for the present and reconstructed ice and land surfaces from the southern dome-derived drainage of David Glacier. The bold lines and their associated values represent the profiles [along the dotted line on (A)] with erosion-corrected ^{10}Be ages for Ricker Hills (Strasky et al., 2009) and Mt. Priestley (this study), while dashed lines show iso-age profile between them. Ages in brackets are the uncorrected ^{21}Ne ages for Ford Peak and Mt. Bowen (Oberholzer et al., 2008).

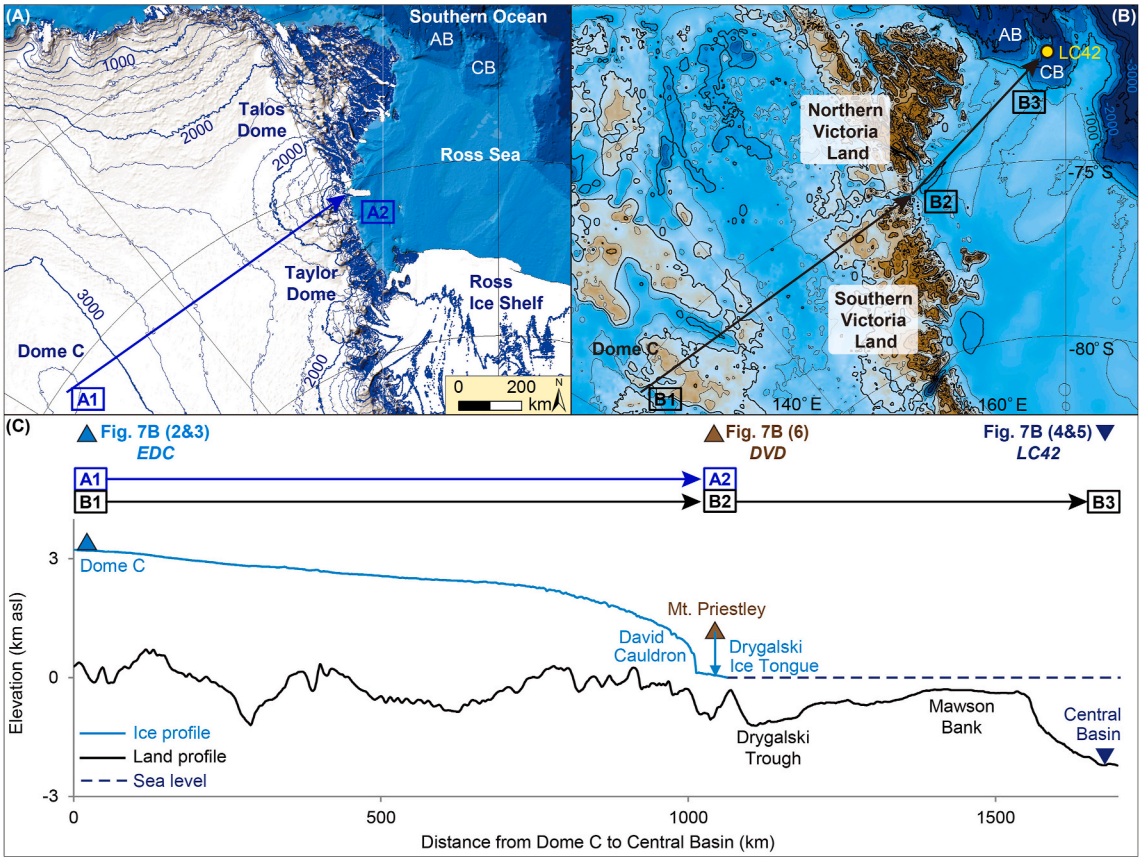

Fig. 6. (A) Present ice surface contour from Dome C to Drygalski ice tongue via Reference Elevation Model of Antarctica (REMA; Howat et al., 2019). Blue arrows follow the flowline of the ice from the Dome C (A1) to the David Cauldron (A2). (B) Subglacial topography and bathymetry map based on the International Bathymetric Chart of the Southern Ocean (IBCSO) Version 1.0 (Arndt et al., 2013). Yellow circle is the location of sediment core (RS15-LC42) from the Central Basin (CB), which is situated nearby the Adare Basin. Black arrows show the bed profile section from the Dome C (B1), through the David Cauldron (B2), and to the Central Basin (B3). (C) Present ice surface (sky-blue line) and subglacial topography/bathymetry (black line) along the Dome C–David Glacier–Central Basin (Fig. 6B; B1–B3). Historical accumulation of David Glacier derived from the deep ice core at Dome C (EDC 3; Figs. 7B–2 and 3; Jouzel et al., 2007; Parrenin et al., 2007). Ablation data and inferred deglaciations are determined from the bedrock/erratics on Mt. Priestley (DVD; Figs. 7B–6) and are compared with sediment cores in the Central Basin (LC42; Figs. 7B–4 and 5; Dash et al., 2021).

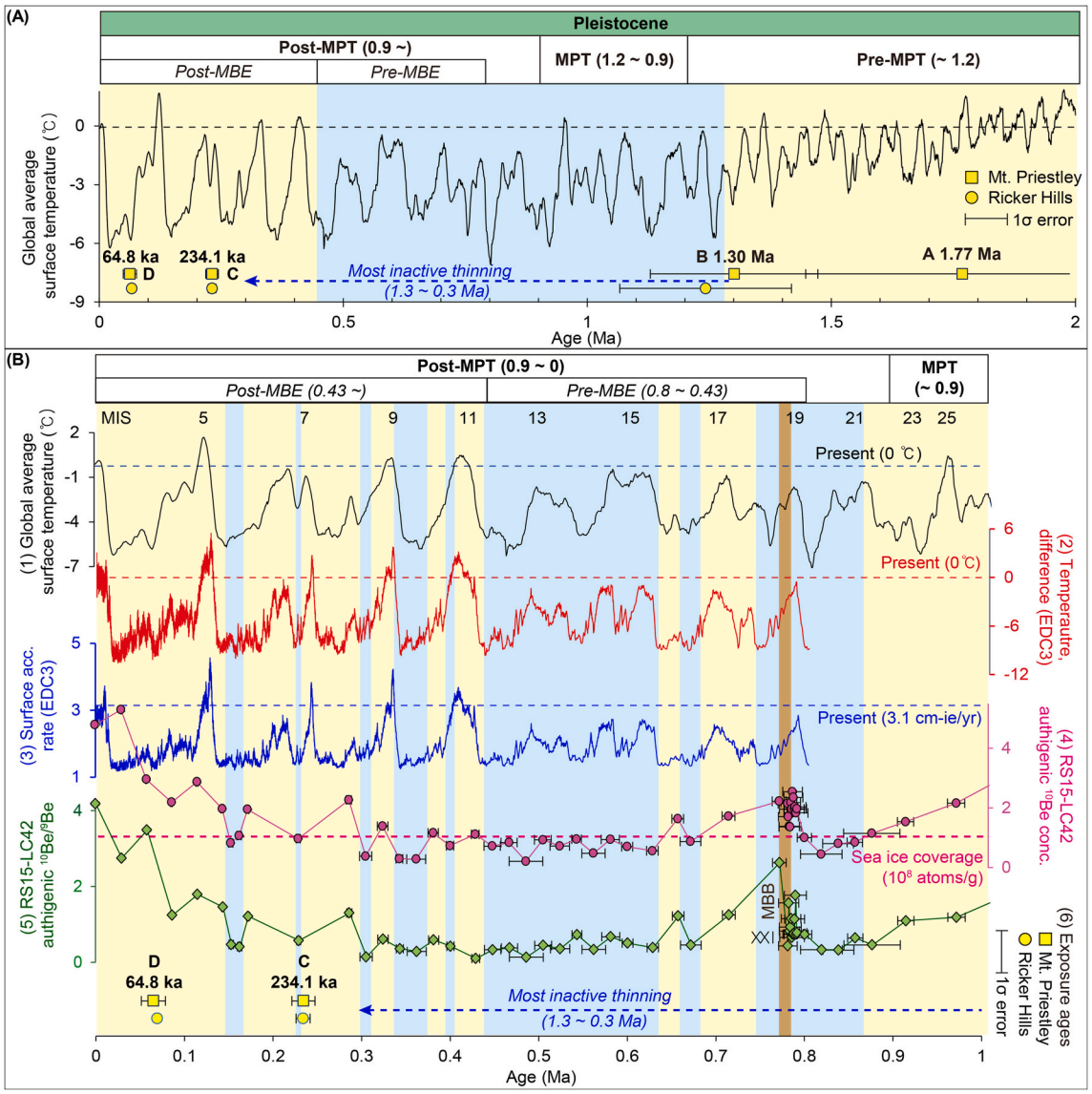

Fig. 7. (A) Global average surface temperature (GAST) changes based on deep sea oxygen isotopes over the last 2 Ma (Snyder, 2016) and exposure ages of Mt. Priestley (this study) and Ricker Hills (Strasky et al., 2009). Our EAIS deglaciations coincide with the early Pleistocene warm period (pre-mid-Pleistocene transition, pre-MPT; Thissen et al., 2003) and late Pleistocene warm interglacial periods (post-mid-Bruhnes transition event, post-MBE; Yin, 2013; Wilson et al., 2018). The sky-blue box roughly indicates colder interglacial periods than present, which corresponds well with our least and slowest ice thinning period (1.3–0.3 Ma), which also emerged on Ricker Hills (Strasky et al., 2009). (B) Climate proxy changes during the last 1 Myr. (1) GAST changes. (2) Temperature difference between the interior EAIS temperature history (East Antarctica Dome C, EDC3; Jouzel et al., 2007) and present-day temperature. (3) Surface accumulation rate, in centimeters of ice equivalent per year (EDC3; Parrenin et al., 2007). (4) and (5) Authigenic ^{10}Be concentrations and ^{10}Be/^{9}Be ratios along Long Core 42, collected during the 2015 Ross Sea cruise (Dash et al., 2021). Pink dashed line is a guideline for ^{10}Be concentrations (10^8 atoms/g), which stands for the sea ice openness. (6) Exposure ages of Mt. Priestley (DVD; this study) and Ricker Hills (Strasky et al., 2009). The sky-blue boxes represent periods of authigenic ^{10}Be depletion, which indicate thick sea ice coverage over the ocean surface due to a decrease in temperature that hindered the direct deposition of meteoric ^{10}Be to the seafloor. The yellow boxes indicate seasonally opened periods. The brown box represents a weakened Geomagnetic Dipole Moment (GDM, XXI) period (Matuyama-Brunhes Boundary; MBB), i.e., <20% of the averaged GDM that produced higher authigenic ^{10}Be than the other periods (Simon et al., 2016).

benches indicating simple exposure and a very low denudation rate (~16 cm/Ma). Relative to other outlet glaciers draining into the Terra Nova Bay, David Glacier has undergone a greater degree of surface lowering (~990 m) since the early Pleistocene. Erratic boulders located on benches C and D (545 and 222 m asl, respectively) were exposed at 234.2 ± 13.1 ka (MIS 7) and 64.8 ± 13.7 ka (mid MIS 4), respectively, with no evidence for overriding since the MIS 8 glacial maximum, PGM (MIS 6), and the Last Glacial Period (MIS 4–2), respectively. The glacier surface was higher (>545 m asl) during the MIS 8 glacial maximum than the PGM (222–545 m asl), which is equivalent to the potential elevation during early MIS 4 (>64.8 ka) Local LGM. Furthermore, the surface of David glacier likely lay at a lower elevation (70–222 m asl) during the LGM (~20 ka) than the local LGM.

Thus, we propose that ice growth since the Quaternary was restricted even during the colder glacial periods due to the prevalence of general dry conditions that inhibited ice accumulation. Nonetheless, overall warm periods during the early Pleistocene and extreme interglacial periods during the late Pleistocene caused major deglaciation that exposed benches on Mt. Priestley. We suggest that modeling of glacier dynamics in the future should consider both these deglaciation-dominated records from the ablation zone and ice core data from the accumulation zone to better constrain the glacial history of the EAIS outlet glaciers draining into the western Ross Sea Embayment.

Declaration of competing interest

The authors declare that they have no known competing financial interests or personal relationships that could have appeared to influence the work reported in this paper.

Acknowledgments

This research is supported by Korea Polar Research Institute (PE21090). We were given lots of practical advice and sincere support from Dr. Jong Ik Lee of Korea Polar Research Institute, South Korea during the field trip.

References

Anderson, J.T., Wilson, G.S., Fink, D., Lilly, K., Levy, R.H., Townsend, D., 2017. Reconciling marine and terrestrial evidence for post LGM ice sheet retreat in southern McMurdo Sound, Antarctica. Quat. Sci. Rev. 157, 1–13.

Arndt, J.E., Schenke, H.W., Jakobsson, M., Nitsche, F.O., Buys, G., Goleby, B., Rebesco, M., Bohoyo, F., Hong, J.K., Black, J., Greku, R., Udintsev, G., Barrios, F., Reynoso-Peralta, W., Taisei, M., Wigley, R., 2013. The International Batyhmetric Chart of the Southern Ocean (IBCSO) Version 1.0 - a new bathymetric compilation covering circum-Antarctic waters. Geophys. Res. Lett. 40, 3111–3117.

Balco, 2016. Saturated Surfaces in Antarctica. https://cosmognosis.wordpress.com/2016/09/09/saturated-surfaces-in-antarctica/.

Balco, 2019. Stone (2000) Revisited. https://cosmognosis.wordpress.com/2019/02/05/stone-2000-revisited.

Balco, G., Schaefer, J.M., LARISSA Group, 2013. Exposure-age record of Holocene ice sheet and ice shelf change in the northeast Antarctic Peninsula. Quat. Sci. Rev. 59, 101–111.

Balco, G., Stone, J.O., Lifton, N.A., Dunai, T.J., 2008. A complete and easily accessible means of calculating surface exposure ages or erosion rates from 10Be and 26Al measurements. Quat. Geochronol. 3 (3), 174–195.

Balter, K., Bromley, G., Balco, G., Thomas, H., Margaret, S.J., 2020. A 14.5-million-year record of East antarctic ice sheet fluctuations from the central transantarctic mountains, constrained with cosmogenic ^{3}Be, ^{10}Be, ^{21}Ne, and ^{26}Al. Cryosphere 14, 2647–2672.

Baroni, C., 1987. Geomorphological map of the northern foothills near the Italian station, (Terra Nova bay, Antarctica). Mem. Soc. Geol. Ital. 33, 195–211, 1987.

Baroni, C., Frezzotti, M., Salvatore, M.C., Meneghel, M., Tabacco, I.E., Vittuari, L., Bondesan, A., Biasini, A., Cimbelli, A., Orombelli, G., 2004. Antarctic Geomorphological and Glaciological 1:250,000 map series. Mt. Murchison Quadrangle (northern Victoria Land). Explanatory notes. (with geomorphological map at the scale of 1:250,000). Ann. Glaciol. 39, 256–264.

Baroni, C., Noti, V., Ciccacci, S., Righini, G., Salvatore, M.C., 2005. Fluvial Origin of the valley system in northern Victoria Land (Antarctica) from quantitative geomorphic analysis. Geol. Soc. Am. Bull. 117 (1–2), 212–228.

Bockheim, J.G., Hall, K.J., 2002. Permafrost, active-layer dynamics and periglacial environments of continental Antarctica: periglacial and permafrost research in the Southern Hemisphere. South Afr. J. Sci. 98 (1), 82–90.

Christ, A.J., Bierman, P.R., 2020. The local last glacial maximum in McMurdo Sound, Antarctica: implications for ice-sheet behavior in the Ross Sea embayment. GSA Bulletin 132 (1–2), 31–47.

Clark, P.U., Dyke, A.S., Shakun, J.D., Carlson, A.E., Clark, J., Wohlfarth, B., Mitrovica, J. X., Hostetler, S.W., McCabe, A.M., 2009. The last glacial maximum. Science 325 (5941), 710–714.

Dash, C., Lee, M.K., Seong, Y.B., Rhee, H.H., Lee, J.I., Yoo, K.-C., 2021. 10Be and 10Be/9Be in glaciomarine sediments of Ross Sea, Antarctica: implications for mid-late Quaternary paleoenvironmental changes. J. Geol. Soc. Korea 57 (5) (in press). http://submission.gskorea.or.kr/html/?pmode=print&seq=383.

Denton, G.H., Sugden, D.E., 2005. Meltwater features that suggest Miocene ice-sheet overriding of the transantarctic mountains in Victoria land, Antarctica. Geogr. Ann. Phys. Geogr. 87 (1), 67–85.

Di Nicola, L., Baroni, C., Strasky, S., Salvatore, M.C., Schlüchter, C., Akçar, N., Kubik, P. W., Wieler, R., 2012. Multiple cosmogenic nuclides document the stability of the East Antarctic ice sheet in northern Victoria Land since the late Miocene (5-7 Ma). Quat. Sci. Rev. 57, 85–94.

Di Nicola, L., Strasky, S., Schlüchter, C., Salvatore, M.C., Akçar, N., Kubik, P.W., Christl, M., Kasper, H.U., Wieler, R., Baroni, C., 2009. Multiple cosmogenic nuclides document complex Pleistocene exposure history of glacial drifts in Terra Nova Bay (northern Victoria Land, Antarctica). Quat. Res. 71 (1), 83–92.

Goehring, B.M., Balco, G., Todd, C., Moening-Swanson, I., Nichols, K., 2019. Late-glacial grounding line retreat in the northern Ross Sea, Antarctica. Geology 47 (4), 291–294.

Gosse, J.C., Phillips, F.M., 2001. Terrestrial in situ cosmogenic nuclides: theory and application. Quat. Sci. Rev. 20 (14), 1475–1560.

Heyman, J., Stroeven, A.P., Harbor, J.M., Caffee, M.W., 2011. Too young or too old: evaluating cosmogenic exposure dating based on an analysis of compiled boulder exposure ages. Earth Planet Sci. Lett. 302 (1–2), 71–80.

Howat, I.M., Porter, C., Smith, B.E., Noh, M.-J., Morin, P., 2019. The reference elevation Model of Antarctica. Cryosphere 13, 665–674.

Jackson, M.S., Hall, B.L., Denton, G.H., 2018. Asynchronous behavior of the antarctic ice sheet and local glaciers during and since termination 1, salmon valley, Antarctica. Earth Planet Sci. Lett. 482, 396–406.

Jeong, A., Lee, J.I., Seong, Y.B., Balco, G., Yoo, K.C., Yoon, H.I., Domack, E., Rhee, H.H., Yu, B.Y., 2018. Late Quaternary deglacial history across the Larsen B embayment, Antarctica. Quat. Sci. Rev. 189, 134–148.

Jones, R.S., Mackintosh, A.N., Norton, K.P., Golledge, N.R., Fogwill, C.J., Kubik, P.W., Christl, M., Greenwood, S.L., 2015. Rapid Holocene thinning of an East Antarctic outlet glacier driven by marine ice sheet instability. Nat. Commun. 6, 8910.

Jones, R.S., Small, D., Cahill, N., Bentley, M.J., Whitehouse, P.L., 2019. iceTEA: tools for plotting and analysing cosmogenic-nuclide surface-exposure data from former ice margins. Quat. Geochronol. 51, 72–86.

Jouzel, J., Masson-Delmotte, V., Cattani, O., Dreyfus, G., Falourd, S., Hoffmann, G., Minster, B., Nouet, J., Barnola, J.M., Chappellaz, J., Fischer, H., Gallet, J.C., Johnsen, S., Leuenberger, M., Loulergue, L., Luethi, D., Oerter, H., Parrenin, F., Raisbeck, G., Raynaud, D., Schilt, A., Schwander, J., Selmo, E., Souchez, R., Spahni, R., Stauffer, B., Steffensen, J.P., Stenni, B., Stocker, T.F., Tison, J.L., Werner, M., Wolff, E.W., 2007. Orbital and millennial antarctic climate variability over the past 800,000 years. Science 317 (5839), 793–796.

Joy, K., Fink, D., Storey, B., Atkins, C., 2014. A 2 million year glacial chronology of the Hatherton Glacier, Antarctica and implications for the size of the East antarctic ice sheet at the last glacial maximum. Quat. Sci. Rev. 83, 46–57.

Kaplan, M.R., Licht, K.J., Winckler, G., Schaefer, J.M., Bader, N., Mathieson, C., Roberts, M., Kassab, C.M., Schwarts, R., Graly, J.A., 2017. Middle to late Pleistocene stability of the central East Antarctic ice sheet at the head of Law Glacier. Geology 45 (11), 963–966.

Knudsen, M.F., Egholm, D.L., 2018. Constraining Quaternary ice covers and erosion rates using cosmogenic 26Al/10Be nuclide concentrations. Quat. Sci. Rev. 181, 65–75.

Kohl, C.P., Nishiizumi, K., 1992. Chemical isolation of quartz for measurement of in-situ-produced cosmogenic nuclides. Geochem. Cosmochim. Acta 56 (9), 3583–3587.

Korschinek, G., Bergmaier, A., Faestermann, T., Gerstmann, U.C., Knie, K., Rugel, G., Wallner, A., Dillmann, I., Dollinger, G., Von Gostomski, C.L., Kossert, K., 2010. A new value for the half-life of 10Be by heavy-ion elastic recoil detection and liquid scintillation counting. Nucl. Instrum. Methods Phys. Res. Sect. B Beam Interact. Mater. Atoms 268 (2), 187–191.

Lal, D., 1991. Cosmic ray labeling of erosion surfaces: in situ nuclide production rates and erosion models. Earth Planet Sci. Lett. 104 (2–4), 424–439.

Levy, R., Harwood, D., Florindo, F., Sangiorgi, F., Tripati, R., Von Eynatten, H., Gasson, E., Kuhn, G., Tripati, A., DeConto, R., Fielding, C., Field, B., Golledge, N., McKay, R., Naish, T., Olney, M., Pollard, D., Schouten, S., Talarico, F., Warny, S., Willmott, V., Acton, G., Panter, K., Paulsen, T., Taviani, M., SMS Science Team., 2016. Antarctic ice sheet sensitivity to atmospheric CO2 variations in the early to mid-Miocene. Proc. Natl. Acad. Sci. Unit. States Am. 113 (13), 3453–3458.

Levy, R.H., Meyers, S.R., Naish, T.R., et al., 2019. Antarctic ice-sheet sensitivity to obliquity forcing enhanced through ocean connections. Nat. Geosci. 12, 132–137.

Lewis, A.R., Marchant, D.R., Ashworth, A.C., Hemming, S.R., Machlus, M.L., 2007. Major middle Miocene global climate change: evidence from East Antarctica and the transantarctic mountains. Geol. Soc. Am. Bull. 119 (11–12), 1449–1461.

Lewis, A.R., Marchant, D.R., Ashworth, A.C., Hedenäs, L., Hemming, S.R., Johnson, J.V., Leng, M.J., Machlus, M.L., Newton, A.E., Raine, J.I., Willenbring, J.K., Williams, M., Wolfe, A.P., 2008. Mid-Miocene cooling and the extinction of tundra in continental Antarctica. Proc. Natl. Acad. Sci. Unit. States Am. 105 (31), 10676–10680.

Lifton, N., Sato, T., Dunai, T.J., 2014. Scaling in situ cosmogenic nuclide production rates using analytical approximations to atmospheric cosmic-ray fluxes. Earth Planet Sci. Lett. 386, 149–160.

Lilly, K., Fink, D., Fabel, D., Lambeck, K., 2010. Pleistocene dynamics of the interior East Antarctic ice sheet. Geology 38 (8), 703–706.

McKay, R., Naish, T., Carter, L., Riesselman, C., Dunbar, R., Sjunneskog, C., Winter, D., Sangiorgi, F., Warren, C., Pagani, M., Schouten, S., Willmott, V., Levy, R., DeConto, R., Powell, R.D., 2012. Antarctic and Southern Ocean influences on late Pliocene global cooling. Proc. Natl. Acad. Sci. Unit. States Am. 109 (17), 6423–6428.

Nishiizumi, K., Imamura, M., Caffee, M.W., Southon, J.R., Finkel, R.C., McAninch, J., 2007. Absolute calibration of 10Be AMS standards. Nucl. Instrum. Methods Phys. Res. Sect. B Beam Interact. Mater. Atoms 258 (2), 403–413.

Oberholzer, P., Baroni, C., Salvatore, M.C., Baur, H., Wieler, R., 2008. Dating late-Cenozoic erosional surfaces in Victoria Land, Antarctica, with cosmogenic neon in pyroxenes. Antarct. Sci. 20 (1), 89–98.

Oberholzer, P., Baroni, C., Schaefer, J.M., Orombelli, G., Ivy Ochs, S., Kubik, P.W., Baur, H., Wieler, R.C., 2003. Limited pliocene/pleistocene glaciation in deep freeze range, northern Victoria land, Antarctica, derived from in situ cosmogenic nuclides. Antarct. Sci. 15 (4), 493–502.

Ohneiser, C., Yoo, K.C., Albot, O.B., Cortese, G., Riesselman, C., Lee, J.I., McKay, R., Bollen, M., Lee, M.K., Moon, H.S., Kim, S.H., Beltran, C., Levy, R., Wilson, G.S., 2019. Magneto-biostratigraphic age models for Pleistocene sedimentary records from the Ross Sea. Global Planet. Change 176, 36–49.

Orombelli, G., Baroni, C., Denton, G.H., 1990. Late cenozoic glacial history of the Terra Nova bay region, northern Victoria land, Antarctica. Geografia Fisica eDinamica Quaternaria 13 (2), 139–163.

Parrenin, F., Barnola, J.-M., Beer, J., Blunier, T., Castellano, E., Chappellaz, J., Dreyfus, G., Fischer, H., Fujita, S., Jouzel, J., Kawamura, K., Lemieux-Dudon, B., Loulergue, L., Masson-Delmotte, V., Narcisi, B., Petit, J.-R., Raisbeck, G., Raynaud, D., Ruth, U., Schwander, J., Severi, M., Spahni, R., Steffensen, J.P., Svensson, A., Udisti, R., Waelbroeck, C., Wolff, E., 2007. The EDC3 chronology for the EPICA Dome C ice core. Clim. Past Discuss 3, 575–606.

Rhee, H.H., Lee, M.K., Seong, Y.B., Hong, S., Lee, J.I., Yoo, K.C., Yu, B.Y., 2019. Timing of the local last glacial maximum in Terra Nova Bay, Antarctica defined by cosmogenic dating. Quat. Sci. Rev. 221, 105897.

Rhee, H.H., Lee, M.K., Seong, Y.B., Lee, J.I., Yoo, K.C., Yu, B.Y., 2020. Post-LGM dynamic deglaciation along the Victoria Land coast, Antarctica. Quat. Sci. Rev. https://doi.org/10.1016/j.quascirev.2020.106595.

Seong, Y.B., Dorn, R.I., Yu, B.Y., 2016. Evaluating the life expectancy of a desert pavement. Earth Sci. Rev. 162, 129–154.

Simon, Q., Thouveny, N., Bourlès, D.L., Valet, J.P., Bassinot, F., Ménabréaz, L., Guillou, V., Choy, S., Beaufort, L., 2016. Authigenic 10Be/9Be ratio signatures of the cosmogenic nuclide production linked to geomagnetic dipole moment variation since the Brunhes/Matuyama boundary. J. Geophys. Res. Solid Earth 121, 7716–7741.

Snyder, C.W., 2016. Evolution of global temperature over the past two million years. Nature 538 (7624), 226–228.

Staiger, J.W., Marchant, D.R., Schaefer, J.M., Oberholzer, P., Johnson, J.V., Lewis, A.R., Swanger, K.M., 2006. Plio-Pleistocene history of Ferrar Glacier, Antarctica: implications for climate and ice sheet stability. Earth Planet Sci. Lett. 243 (3–4), 489–503.

Strand, K., Passchier, S., Näsi, J., 2003. Implications of quartz grain microtextures for onset Eocene/Oligocene glaciation in Prydz Bay, ODP Site 1166, Antarctica. Palaeogeogr. Palaeoclimatol. Palaeoecol. 198 (1–2), 101–111.

Strasky, S., Di Nicola, L., Baroni, C., Salvatore, M.C., Baur, H., Kubik, P.W., Schlüchter, C., Wieler, R., 2009. Surface exposure ages imply multiple low amplitude Pleistocene variations in East Antarctic ice sheet, Ricker Hills, Victoria Land. Antarct. Sci. 21 (1), 59–69.

Sugden, D., Denton, G., 2004. Cenozoic landscape evolution of the convoy range to Mackay glacier area, transantarctic mountains: onshore to offshore synthesis. Geol. Soc. Am. Bull. 116 (7–8), 840–857.

Sugden, D.E., Denton, G.H., Marchant, D.R., 1991. Subglacial meltwater channel systems and ice sheet overriding, Asgard Range, Antarctica. Geogr. Ann. Phys. Geogr. 73 (2), 109–121.

Sutter, J., Fischer, H., Grosfeld, K., Karlsson, N.B., Kleiner, T., Liefferinge, B.V., Eisen, O., 2019. Modelling the antarctic ice sheet across the mid-pleistocene transition – implications for oldest ice. Cryosphere 13, 2023–2041.

Swanger, K.M., Marchant, D.R., Schaefer, J.M., Winckler, G., Head III, J.W., 2011. Elevated East Antarctic outlet glaciers during warmer-than-present climates in southern Victoria Land. Global Planet. Change 79 (1–2), 61–72.

Thissen, K.M., Dunbar, R.B., Cooper, A.K., Mucciarone, D.A., Hoffmann, D., 2003. The Pleistocene evolution of the East antarctic ice sheet in the prydz bay region: stable istotopic evidence from ODP site 1167. Global Planet. Change 39, 227–256.

Wilson, D.J., Bertram, R.A., Needham, E.F., Flierdt, T.V., Welsh, K.J., McKay, R.M., Mazumder, A., Riesselman, C.R., Jimenez-Espejo, F.J., Escutia, C., 2018. Ice loss from the East antarctic ice sheet during late Pleistocene interglacials. Nature 561 (7723), 383–386.

Wuite, J., Jezek, K.C., Wu, X., Farness, K., Carande, R., 2009. The velocity field and flow regime of David glacier and Drygalski ice tongue, Antarctica. Polar Geogr. 32 (3), 111–127.

Yin, Q., 2013. Insolation-induced mid-Brunhes transition in Southern Ocean ventilation and deep-ocean temperature. Nature. Feb 14 494 (7436), 222–225.